Electronic Supplementary Material (ESI) for Chemical Communications.

Electronic Supplementary Information (ESI)

Electronic Interplay: Synergism of Binary Transition Metals and Role of M-N-S Site Towards Oxygen Electrocatalysis

Manisha Das†, Ashmita Biswas† and Ramendra Sundar Dey*

† These authors contributed equally.

Institute of Nano Science and Technology (INST), Sector-81, Mohali-140306, Punjab, India.

*Email: rsdey@inst.ac.in

Table of content

ESI 1. Experimental

ESI 2. Figures

ESI 4. Tables

1. Experimental

1.1 Chemicals: Iron (II) sulphate heptahydrate ($FeSO_4.7H_2O$), Cobalt (II) Chloride hexahydrate ($CoCl_2.6H_2O$), Zinc acetate, Potassium hydroxide, Dopamine, L-cysteine, Pt/C (20 wt %) and RuO_2 were purchased from Sigma Aldrich and were used as received. Hydrochloric acid (HCl) was purchased from Merck chemicals India. All other reagents used in this study were of pure analytical grade and were used without any further purification.

1.2 Synthesis of FeCoDACys catalyst: In this work, we designed a carbonaceous electrocatalyst based on Fe-Co dual site coordinated with N and S as co-dopant, where dopamine and cysteine served as the source of N and S respectively. The synthesis of FeCoDACys electrocatalyst was done by grinding the mixture of dopamine, L-cystine, $FeSO_4.7H_2O$ and $CoCl_2.6H_2O$ using a mortar and pestle in a proportionate amount Fe:Co:Da:Cys (0.4:0.6:1:0.2) in molar ratios, followed by pyrolysis at 800°C for 2 h in an argon atmosphere (99.99%) at a constant heating rate of 3°C min^{-1}. The pyrolyzed sample was then ball milled at 300 rpm for 30 min to form a uniformly grinded fine powder. The obtained sample after ball milling was then washed with dilute HCl (6M) for 10 times to remove the inactive Fe and Co particles from the sample. The sample was then followed by the stepwise washing with Milli-Q water, until a neutral pH was attained and finally dried in a hot air oven at 60°C for 24 h. For the comparison of the activity and to understand the mechanism, FeDACys and CoDACys were also synthesized using the same protocol as stated above. This method enabled us to have a precise control over the local coordination of the active site to achieve S-N-M_1-M_2-N-S architecture in the carbon framework, which favored the adsorption of H_2O and O_2 during the OER and ORR processes respectively.

1.3 Physical characterizations: X-ray diffraction (XRD) pattern was obtained on a Bruker D8 Advances instrument using Cu-Kα (λ = 1.5406 Å) radiation with an acceleration voltage of 40KV in the 2θ range from 10° to 80°. The surface morphological characterization and the determination of elemental composition of all the prepared catalyst samples were investigated using Scanning Electron Microscopy (SEM Jeol JSMIT300) equipped with a Bruker XFlash 6130 Energy Dispersive X-ray Spectroscopy (EDS). Transmission Electron Microscopy (TEM) analysis was carried out on a JEM2100 instrument suitable for High-Resolution TEM (HRTEM) studies. X-ray photoelectron spectroscopy (XPS) with an ultrahigh vacuum chamber (2×10^{-9} mbar) using (Monchromatic) with 6 mA beam current by Kα plus XPS system by ThermoFisher Scientific instruments (UK) were recorded to know the chemical states of the sample. All the pH condition of the solution was done using Eutech pH meter instrument. The Extended X-ray absorption fine structure spectra (EXAFS) were carried out with the dispersive EXAFS beam line (BL-9) at Indus-2 synchrotron radiation source at the Raja Ramanna Centre for Advanced Technology (RRCAT), Indore, India. The measurements were done in transmission mode. The beamline consisted of Rh/Pt coated meridional cylindrical mirror for collimation and a Si (111) double crystal monochromator (DCM) to select excitation energy of Fe and Co K-edges. All the spectra were measured under ambient condition. Data analysis was carried out using DEMETER programs. Athena and Artemis codes were utilised to extract the measured data and fit the profiles. Nitrogen adsorption-desorption analysis was done at 77 K on an Autosorb iQ2 instrumental setup to examine the surface area by Brunauer Emmett Teller (BET) method. The pore size distribution analysis of the sample was carried out with nonlocal density functional theory (NLDFT). Fourier transform Infrared (FTIR) spectroscopy was carried out on an Agilent technology Cary 600 series.

1.4 Electrode fabrication: The glassy carbon, RDE and RRDE electrode were polished with 1, 0.3 and 0.05 µm Alumina (Al_2O_3) powder followed by the cleaning ultrasonically in DI water. The ink of the catalyst was prepared by dispersing the catalyst in a solution containing 1:1 ratio of DI water and isopropyl alcohol (IPA), after which the sonication was done for 30 min. The dropcasting of the ink on electrode was done according to the optimised mass loading of 1.5 mg cm^{-2}. Simultaneously, Pt/C and RuO_2 electrode was prepared as a reference for comparing the activity of the sample using by adding Pt/C (20 wt %) in of milli-Q water, ethanol and Nafion (5%) to get the desired ink.

1.5 Zinc-air battery set-up: The homemade Zn-Air Battery were assembled using a two-electrode configuration, where the catalyst FeCoDACys served as the cathode, for oxygen evolution reaction (OER) and oxygen reduction reaction (ORR) for charging and discharging, polished Zn foil of 0.25 mm was used as the anode, and 6 M KOH solution with 0.2 M zinc acetate as an electrolyte. The dropcasting of FeCoDACys catalyst was done on the nickel foam (1 × 1) cm^2 electrodes to prepare catalyst ink which was used as current collector with a mass loading of 1.5 mg cm^{-2}.

1.6 Electrochemical measurements: All the electrochemical characterizations were performed using three electrode system using Ag/AgCl (3 M KCl) as reference electrode, graphite rod (diameter = 10 mm) as counter electrode and glassy carbon electrode (GCE, diameter = 3 mm)/RDE/RRDE as working electrode. The measurements were done employing rotating disk electrode (RDE, diameter = 3 mm) and rotating ring disk electrode (RRDE, diameter = 5 mm) in a Metrohm Multi Autolab/M204, while few electrochemical measurements were carried out in CHI 760E Electrochemical Workstation. For the analysis of electrochemical studies, cyclic voltammetry (CV) and linear sweep voltammetry (LSV) tests were carried out in a 0.1 M KOH electrolyte after the purging of O_2 gas for 30 min. The obtained scan potential using Ag/AgCl (3 M KCl) as reference electrode was converted into the reversible hydrogen electrode (RHE) using the equation 1, following the Nernst equation as:

E_{RHE} (V) = $E_{\text{Ag/AgCl (3 M KCl)}}$ (in V) + (0.058 × pH) + 0.210 V (1)

The calculation for the number of electron (n) and hydrogen peroxide (%H_2O_2) during ORR which the catalyst possesses was analyzed using RRDE measurements using

equation 2 and 3, (2)

$$n = 4 \times \frac{I\text{D}}{I\text{D} + \frac{I\text{R}}{N}}$$

(3)

$$\%H2O2 = 200 \times \frac{\frac{I\text{R}}{N}}{\frac{I\text{R}}{N} + I\text{D}}$$

where I_{D} and I_{R} represent the disk and ring current, respectively. N accounts to the collection efficiency of Pt ring, which is (N=0.249) in this case.

The J_K value can be analyzed on the basis of Koutecky-Levich (K-L) formula using equation 45 and 6,

$$\frac{1}{\ } + \frac{1}{J\text{K}}$$

$$\frac{1}{J} = \frac{1}{J\text{L}} + \frac{1}{J\text{K}{=}B\omega^{\frac{1}{2}}} \qquad (4)$$

$$B{=}0.62nFC0\ D0^{2/3}\vartheta^{-1/6} \qquad (5)$$

$$J\text{K} = \text{nFk}C0 \qquad (6)$$

J is the current density, J_K and J_L are the kinetic and diffusion-limiting current densities, ω is the angular velocity of the disk (ω = 2πN, N is the linear rotation speed), n is the overall number of electrons transferred in O_2 reduction, F is the Faraday constant (F = 96485 C mol^{-1}), C_0 is the bulk concentration of O_2, ϑ is the kinematic viscosity of the electrolyte, D_0 is the diffusion coefficient of O_2 in 0.1 M KOH ($D_0 = 1.9\times10^{-5}$ $\text{cm}^2\ \text{s}^{-1}$), and k is the electron transfer rate constant. The n value and J_K can be obtained from the slope and intercept of the Koutecky–Levich plots, respectively.

1.7 Reactions involved:

OER:

The thermodynamics of OER in alkaline media involves the equations as:

$$OH^- + \ * \rightarrow OH_{ads} + e^-$$

$$OH_{ads} + OH^- \rightarrow O_{ads} + H_2O + e^-$$

Where * is catalyst active site and O_{ads} is the adsorbed oxygen on the catalyst surface. There are basically two pathways for the production of O_2 from the oxygen adatoms which are adsorbed on the catalytic active sites.

The first pathways are occurring when the two O_{ads} couples with one another.

$$O_{ads} + O_{ads} \rightarrow O_2$$

And in the next step the O_{ads} reacts with OH^- to form intermediate OOH_{ads} species which finally combines with OH^- to produce O_2.

$$O_{ads} + OH^- \rightarrow OOH_{ads} + e^-$$

$$OOH_{ads} + OH^- \rightarrow O_2 + H_2O + e^-$$

ORR:

The reaction occurs at the cathode during oxygen reduction reaction in an aqueous electrolyte of fuel cell or metal air batteries goes through four main steps: (a) the diffusion and the adsorption of the O_2 molecules at the electrocatalyst surface, (b) transfer of electrons from anode to the adsorbed O_2 molecules, (c) breaking of the oxygen bonds (O=O), and (d) removal of the generated OH- ion to the solution. The reaction for the oxygen reduction to OH- may follow an efficient four-electron pathway in a single step or two-electron pathway which is sluggish and involves two steps:

$O_2 + H_2O + 4e^- \rightarrow 4OH^- (0.401\ V\ vs\ SHE)$

$O_2 + H^+ + 4e^- \rightarrow H_2O \quad (1.229\ V\ vs\ SHE)$

Where, SHE is standard hydrogen electrode.

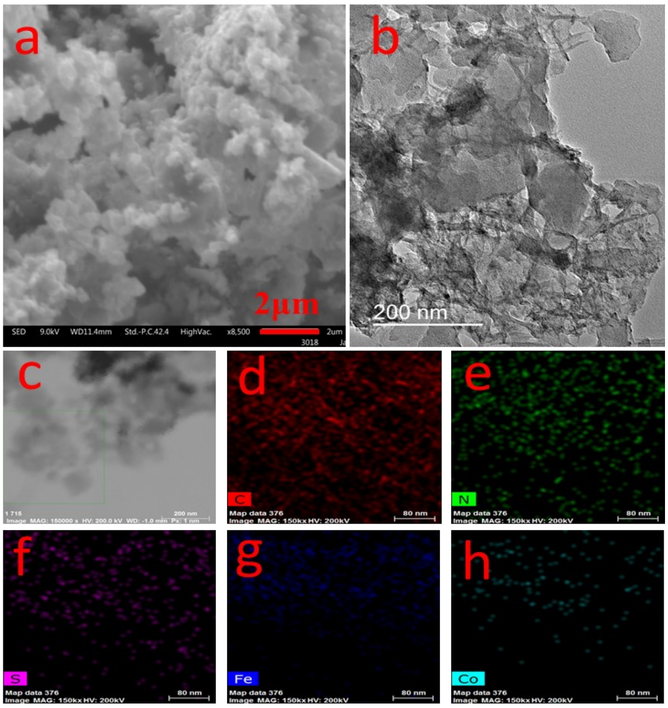

Figure S1. (a-b) SEM image of FeCoDACys at a magnification of 2 μm and 200 nm respectively; (c-h) Corresponding elemental mapping of the catalyst taken from SEM.

Figure S1a illustrates the morphological characterization of the as prepared samples was done with the help of scanning electron microscopy (SEM). The SEM image of FeCoDACys catalyst (S1 a-b) demonstates entangled graphene like sheets. The presence of Fe, Co, S, N and C in the sample was estimated with the help of elemental mapping as shown in Figure S1 c-h.

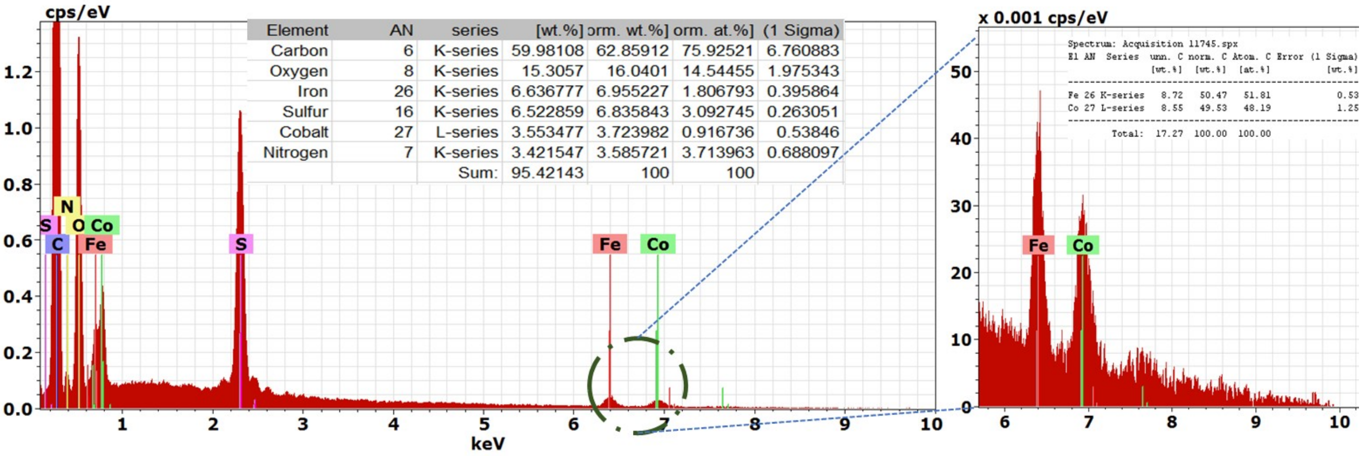

Element	AN	series	[wt.%]	orm. wt.%]	orm. at.%]	(1 Sigma)
Carbon	6	K-series	59.98108	62.85912	75.92521	6.760883
Oxygen	8	K-series	15.3057	16.0401	14.54455	1.975343
Iron	26	K-series	6.636777	6.955227	1.806793	0.395864
Sulfur	16	K-series	6.522859	6.835843	3.092745	0.263051
Cobalt	27	L-series	3.553477	3.723982	0.916736	0.53846
Nitrogen	7	K-series	3.421547	3.585721	3.713963	0.688097
		Sum:	95.42143	100	100	

```
Spectrum: Acquisition 11745.spx
El AN  Series   unn. C norm. C Atom. C Error (1 Sigma)
                [wt.%]  [wt.%]  [at.%]          [wt.%]
------------------------------------------------------
Fe 26 K-series   8.72   50.47   51.81             0.53
Co 27 L-series   8.55   49.53   48.19             1.25
------------------------------------------------------
        Total:  17.27  100.00  100.00
```

Figure S2. EDAX mapping for the elements present in the FeCoDACys electrocatalyst showing carbon, nitrogen, sulphur, iron, cobalt and oxygen.

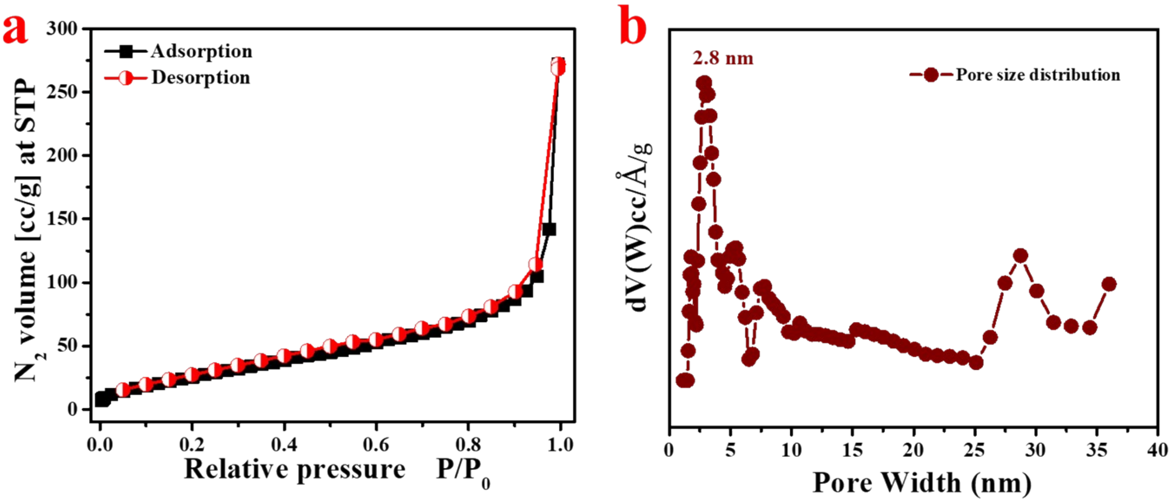

Figure S3: (a) BET adsorption-desorption isotherm (b) Pore size distribution of FeCoDACys catalyst.

FeCoDACys material possess mesoporosity, which was confirmed from N_2 adsorption-desorption isotherm (Figure S3). The graph displays type IV isotherm with a hysteresis loop in the higher relative pressure region (P/P_0) along with a steep increment of adsorption capacity in 0.9-1 range of relative pressure (P/P_0) indicating the co-existence of mesoporosity and interparticle porosity in the sample (Figure S3a). The pore size distribution curve was obtained from the isotherm empolying nonlocal density functional theory (NLDFT) which ensures the presence of mesopores (2.8 nm) in FeCoDACys sample as shown in Figure S3b. The Brunauer–Emmett–Teller (BET) surface area of FeCoDACys catalyst was calculated to be 105 m^2g^{-1}.

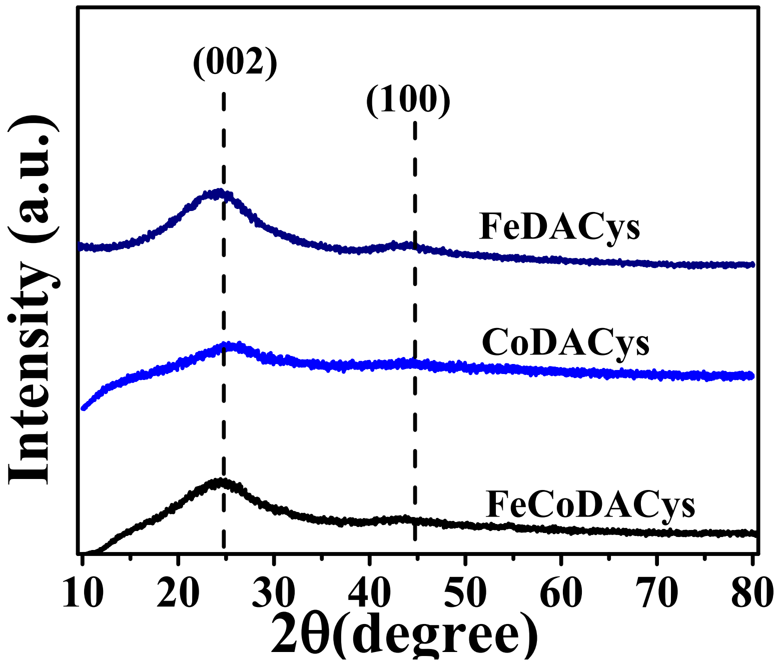

Figure S4. X-ray diffractometry for FeCoDACys sample including all the control samples.

The crystalline structure of FeCoDACys sample along with the other control samples were analysed by X-ray diffractometer (XRD) which is displayed in Figure S4. The samples exhibit expected two broad diffraction peaks around 24°-25° and 44°-45°, attributed to (002) and (100) which corresponds to the low graphitization of the carbon lattice present in the sample.[1,2] The XRD spectra does not indicated the presence of any metallic (Fe, Co) peak present in the sample, which confirms the fine washing of metallic impurities which was present in the sample. Moreover, the peaks present in FeCoDACys catalyst is broader as compared to other control samples, indicating the doping of Fe, Co, N and S in the carbon matrix induce more defect and disordered sites in the carbon structure.

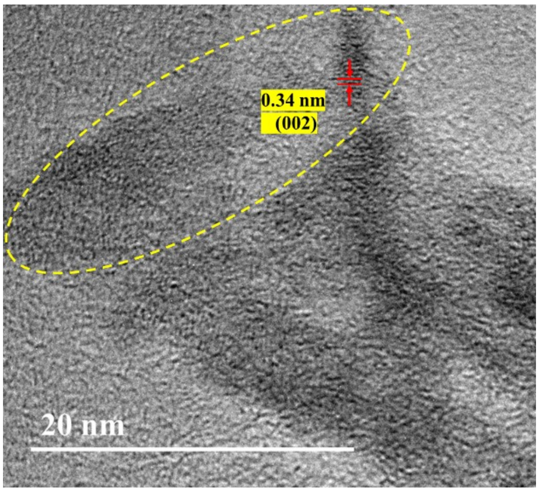

Figure S5: HRTEM image of FeCoDACys catalyst showing the fringe-width for carbon (002) plane.

The high resolution (HR)-TEM image of the catalyst in Figure S5 displays lattice fringes corresponding to a width of 0.34 nm for the (002) plane of the carbon matrix.

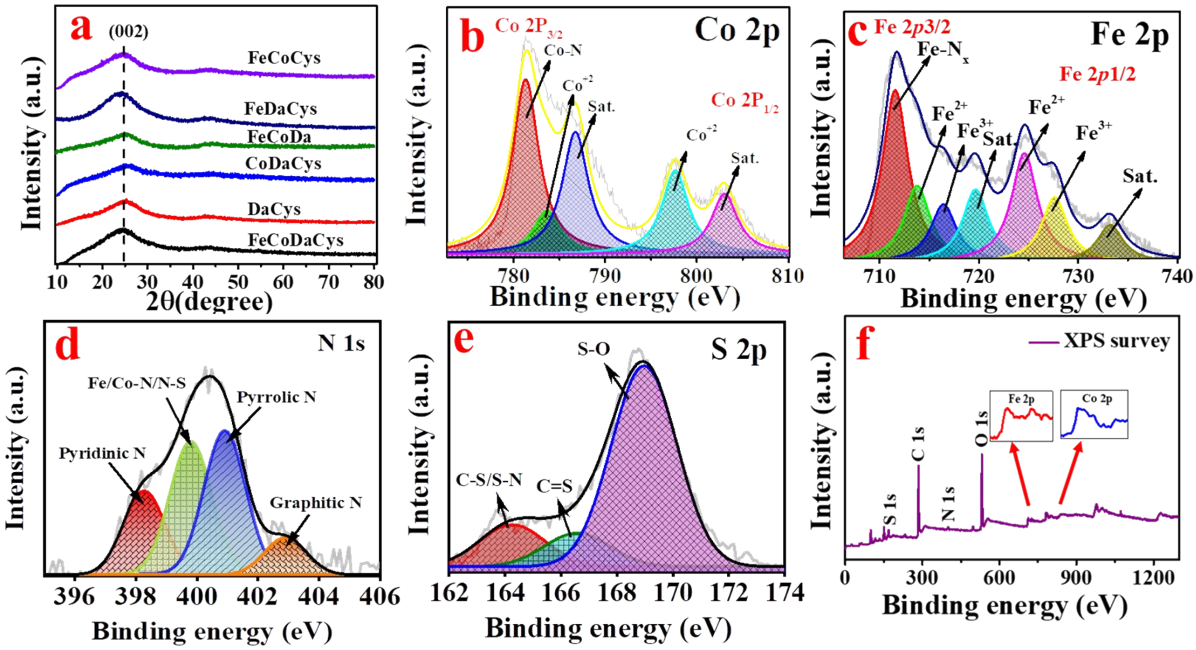

Figure S6. XPS for different elements present in the as prepared bifunctional electrocatalyst FeCoDACys (a) Carbon (b) Cobalt (c) Iron (d) Nitrogen (e) Sulphur (f) XPS survey.

X-ray photoelectron spectroscopy (XPS) was performed to measure the chemical composition and oxidation state of FeCoDACys catalyst. The XPS survey scan depicted the presence of C, N, S, Fe and Co elements in the catalyst. High resolution spectra for C 1s is shown in Figure S6a, which shows the peaks present at 284.17, 285.77, 288.54 and 291.44 eV corresponds to C=C, C=N, C-O and -O-C=O bond. [3,4] The high-resolution Co 2p spectra of FeCoDACys (Figure S6b), shows that the spectrum being deconvoluted into different peaks, the peak at 781.27 and 783.62 eV in Co $2p_{3/2}$ and at 797.62 eV in Co $2p_{1/2}$ is due to Co^{+2}/ Co^{+3} because of the coordination of Co with O or N ions which is very likely due to Co-Nx formation which was further confirmed through EXAFS data. Meanwhile, the peak present at 786.72 and 803.13 eV for Co $2p_{1/2}$ is the shake-up satellite peak is the sign of Co-OH/Co-O formation, which indicates the formation of partial oxidation on the surface of FeCoDACys catalyst which might be occurred due to atmospheric exposure.[5,6] However, the presence of oxide peaks was not evidenced in the XRD characterization, which confirms the oxide formation is due to the surface oxidation. The spectrum corresponding Fe 2p was deconvoluted into six different peaks as shown in Figure S6c. The peaks at 711.49 and 713.84 eV for Fe $2p_{3/2}$ and the peaks at 724.59 and 727.56 eV for Fe $2p_{1/2}$ are attributed for Fe^{2+} and Fe^{3+}, respectively which is mainly due the presence of FeN bond. [7,8] The deconvolution of high-resolution N 1s spectra shows the four distinct peaks at 398.37 eV for Pyridinic N (CN=C), 399.6 eV for the coordination of Fe/Co-N_x

bond and N-S bond, 400.43 eV for tertiary N [N-$(C)_3$] and 401.54 eV for the confirmation of amino (N-H) bond (Figure S6d). [9,10]The S 2p signal was further deconvoluted into three peaks as depicted in Figure S6e. The peaks at 164.12 and 166.52 eV are corresponding to the presence of bond between carbon and sulphur C-S/S-N and C=S, respectively. The analysis for the present of all the elements with their bonds and chemical environment was obtained from XPS, which reflects from XPS survey (Figure S6f).

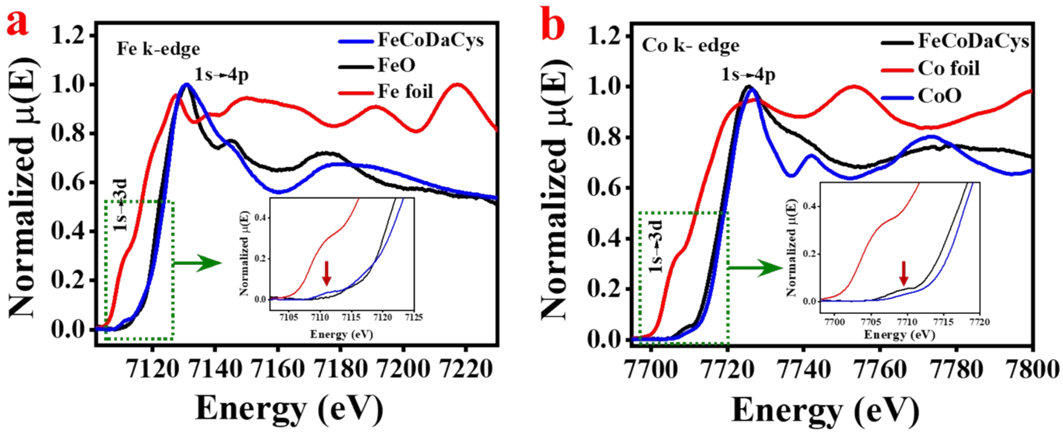

Figure S7: The normalized XANES spectra of (a) Fe k-edge (inset shows enlarged pre-edge peaks) and (b) Co k-edge (inset shows enlarged pre-edge peaks) of FeCoDACys and all the standard samples.

The X-ray absorption near edge structure (XANES) spectra of the FeCoDACys catalyst and the reference samples at Fe K-edge reveal that the peak position (absorption edge) for Fe in FeCoDACys almost overlays with that of FeO (Fe^{2+}), indicating a ~ +2 oxidation state of Fe (Figure S7a) in the electrocatalyst. This is alike the XANES spectra of FeCoDACys catalyst at Co K-edge in Figure S7b predicts a similar ~ +2 oxidation state of the Co.

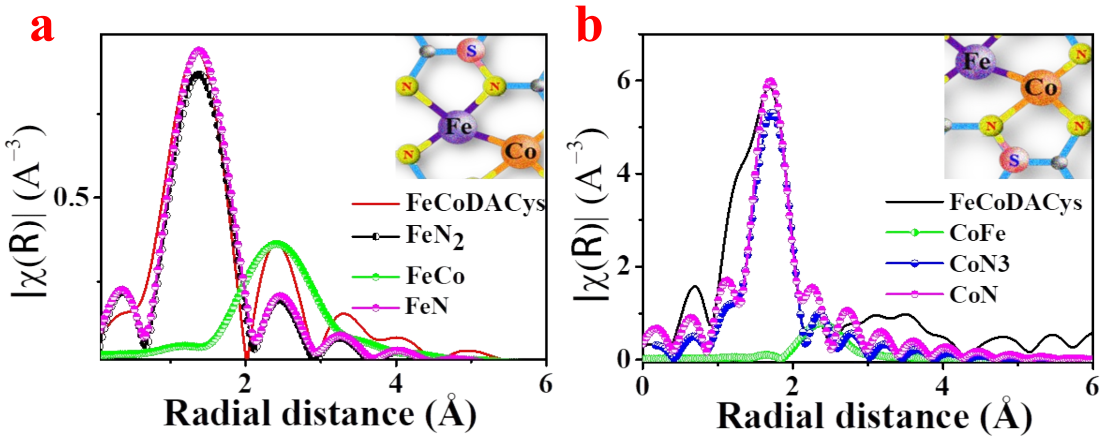

Figure S8. (a) Fitting of FT-EXFAS signal for Fe K-edge (b) The fitting of FT-EXFAS signal for Co K-edge.

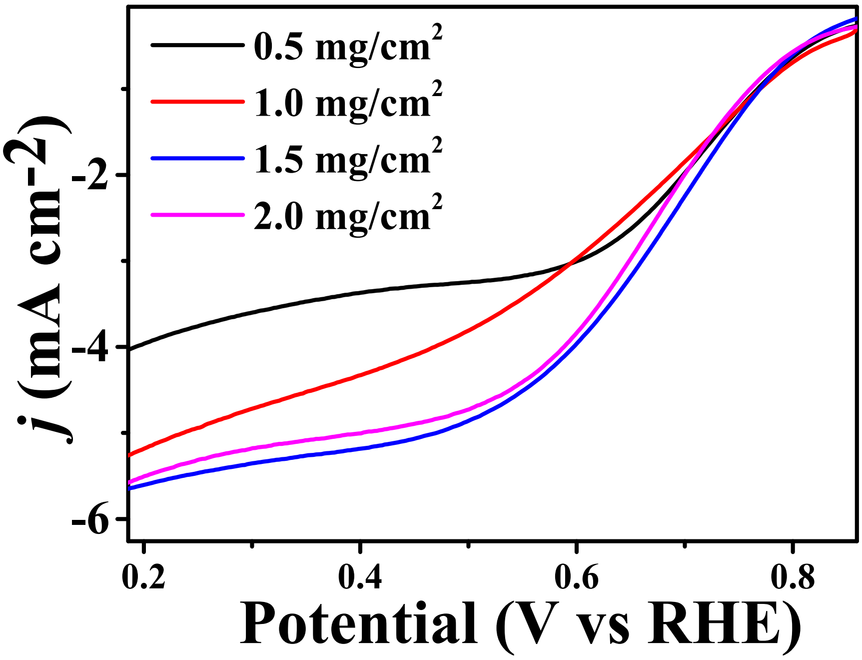

Figure S9. Mass loading optimization of FeCoDACys catalyst toward ORR.

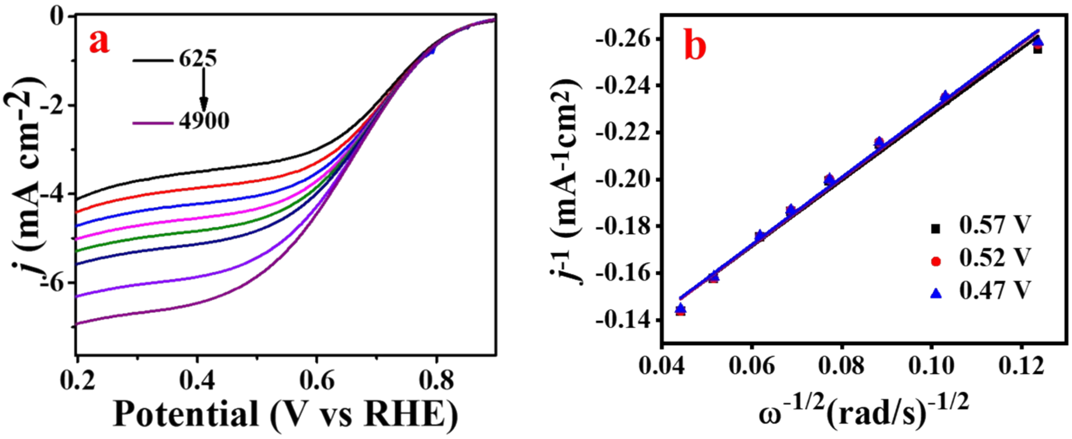

Figure S10. (a) LSV polarisation curve for FeCoDACys electrocatalyst at rotating speed from 625 to 4900 rpm at a scan rate of 10mVs^{-1}; (b) K-L plot of the catalyst at different potentials and rotating speed ranging from 625 to 4900 rpm.

The kinetics of the electrode was determined by taking the LSV scan of FeCoDACys using RDE from 625 to 4900 rpm in O_2 saturated 0.1 M KOH electrolyte as shown in Figure S10a. From LSV curve we obtained the as expected gradual increment in the current density with respect to the rotation which is due to the increased oxygen diffusion at the shortened distance on the electrode surface upon increasing rotation rate. The kinetics of the electrode was further analysed with rotating ring disk electrode (RRDE) to evaluate the Koutecky–Levich (K-L) plot as depicted in Figure 3b, which was extracted from the polarisation curve, showing the linear behaviour at different potential.

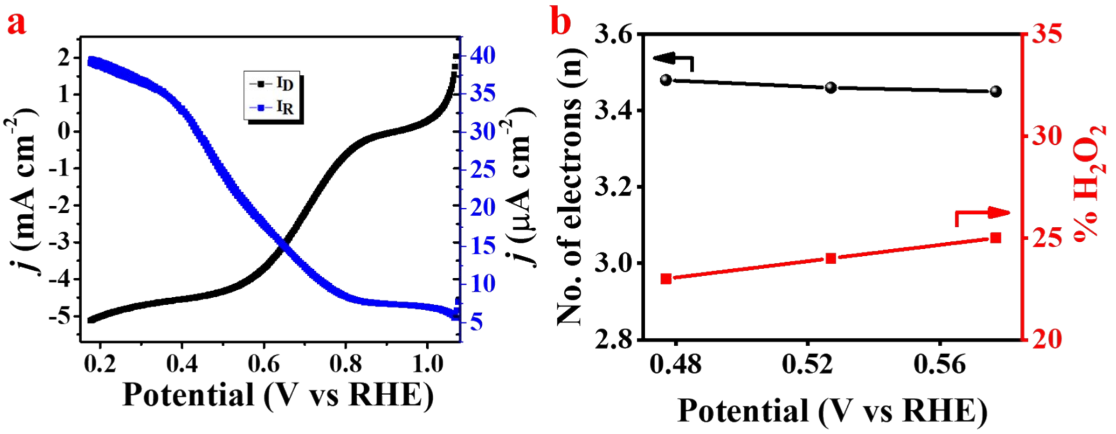

Figure S11. (a) LSV polarization curves of FeCoDACys catalyst corresponding to ring (blue) and disc (black) currents in 0.1 M KOH at 1600 rpm; (b) H_2O_2 tolerance and number of electrons taking part in the ORR for FeCoDACys catalyst.

It has been evaluated that the catalyst follows approximately a direct four electron pathway (Figure S11). H_2O_2 interference, which is a major issue in the ORR reaction was calculated to be around 25 % using the formula (equation 3), which is quite low as compared to the other recently reported data.

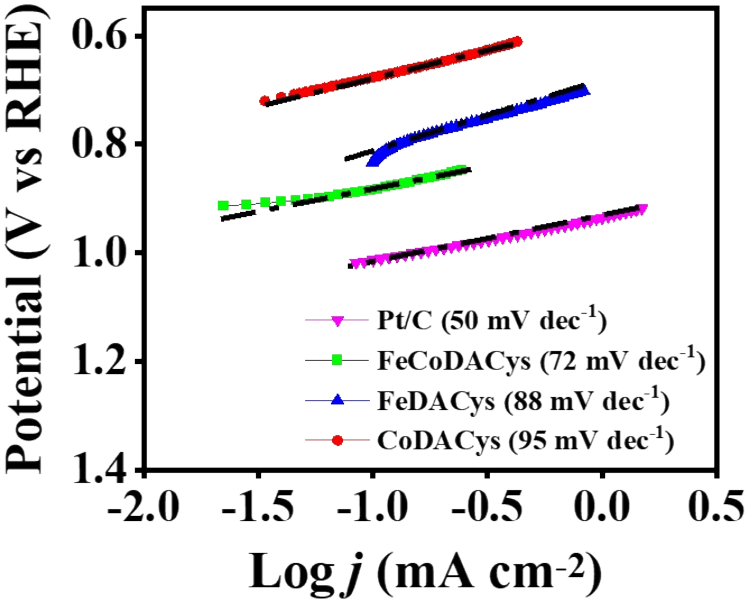

Figure S12: Comparative tafel slope of FeCoDACys, Pt/C and all control catalysts for ORR extracted from LSV polarization curve taken in O_2 saturated 0.1 M KOH solution at 1 mV s^{-1}.

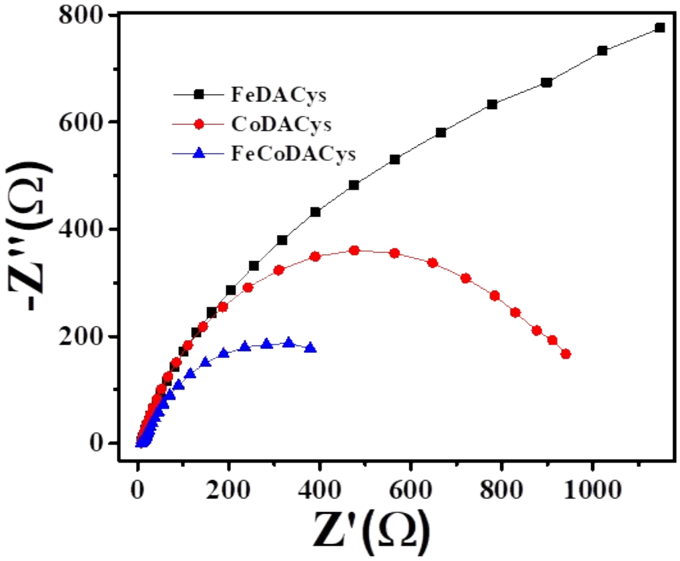

Figure S13: Electrochemical impedance spectra recorded in 0.1 M KOH for all the control samples along with FeCoDACys catalyst.

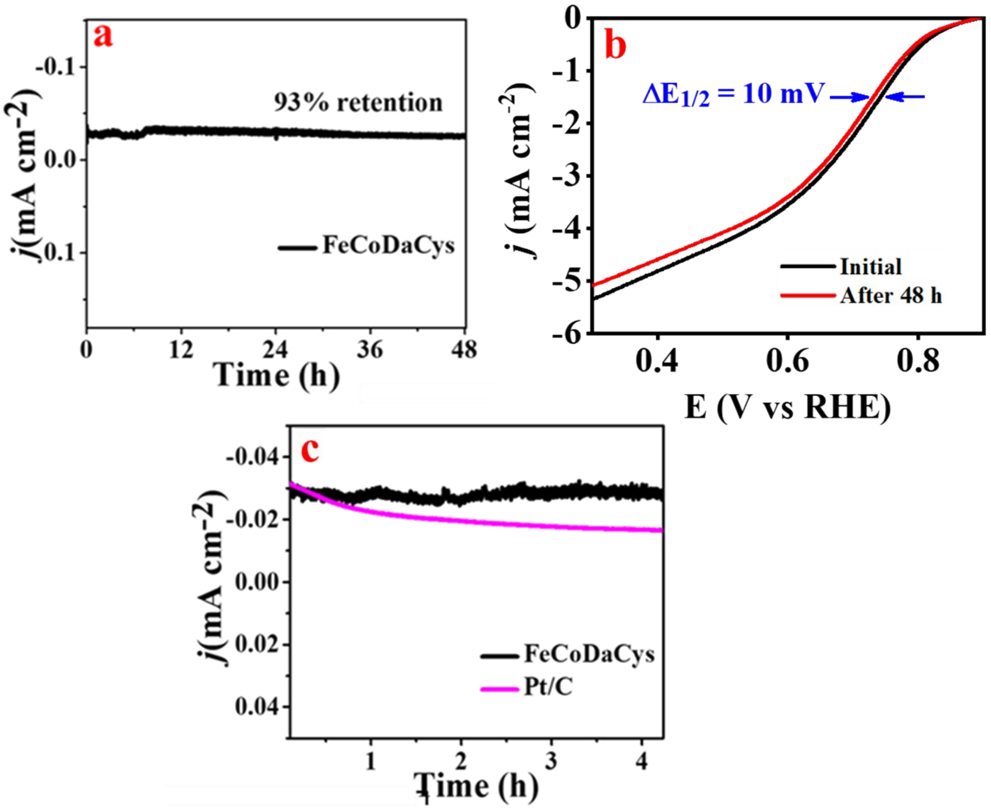

Figure S14. (a) Chronoamperometry to check the stability of the sample for 48 h; (b) LSV for FeCoDACys catalyst before and after stability for 48 h; (c) Comparitive plots showing better stability of FeCoDACys catalyst over the state-of-the-art Pt/C catalyst within ~ 4 h of chronoamperometric run.

The durability of the catalyst was also checked through chronoamperometry (CP) test for 48 h and compared with the benchmark Pt/C catalyst in Figure S13a-c. As expected, FeCoDACys catalyst demonstrated an excellent current retention of 93% after continuous 48 h chronoamperometric run.

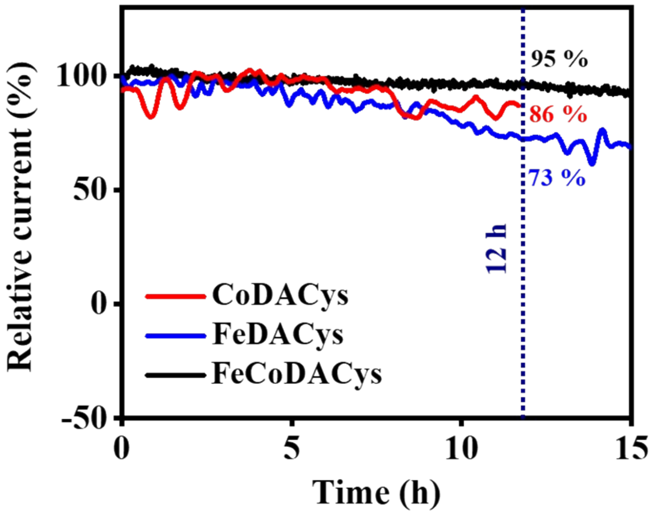

Figure S15: Stability (Chronoamperometry) in terms of relative current (%) of FeDACys, CoDACys and FeCoDACys catalysts towards ORR.

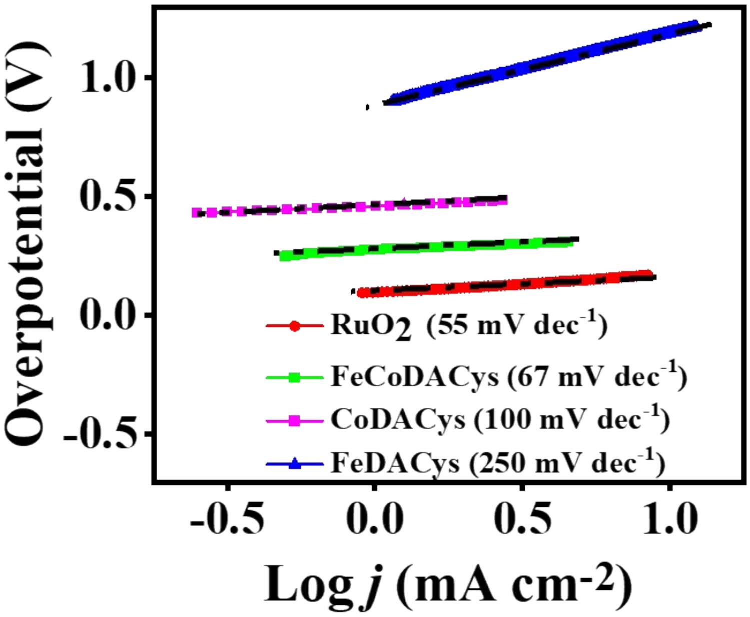

Figure S16: Tafel slope for OER extracted from LSV polarization curves of all the concerned catalysts, taken at 1 mV s^{-1}.

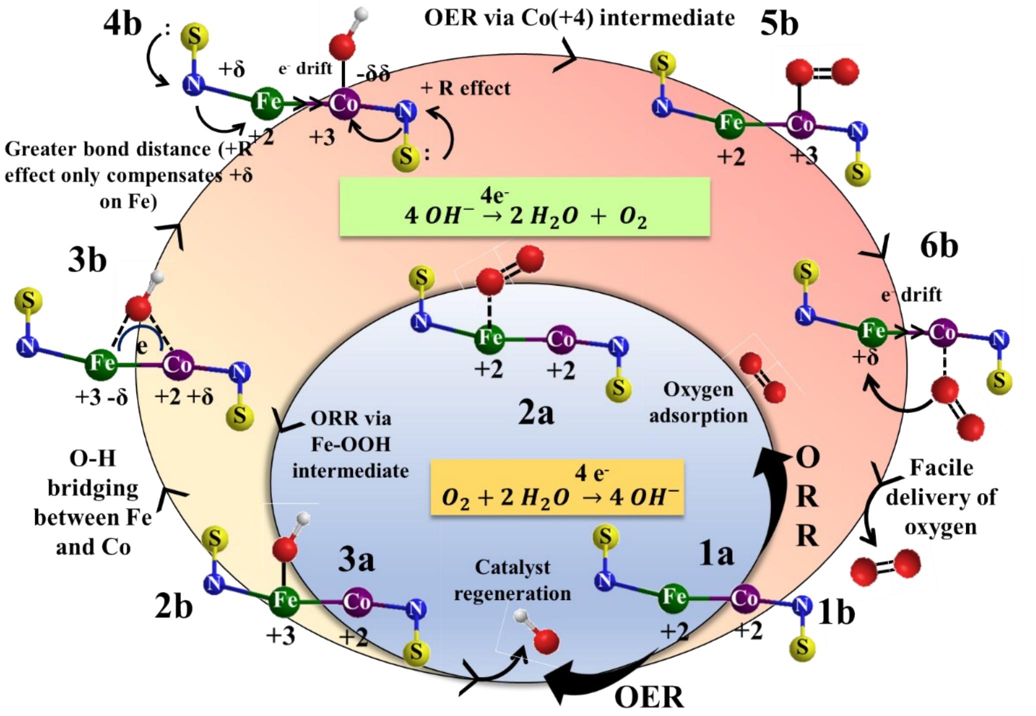

Figure S17: Plausible reaction mechanism of oxygen electrocatalysis (ORR (blue circle) and OER (pink circle)) over active sites of the catalyst.

The catalyst FeCoDACys is consistent with distinct Fe and Co metal centers active toward ORR and OER, respectively, and the catalytic performance increases drastically upon metalation between Fe and Co (Fe-Co binary metal centers).

$$Fe^{3+} + e^- \rightarrow Fe^{2+} \qquad E = +\,0.77\ V$$

$$Co^{3+} + e^- \rightarrow Co^{2+} \qquad E = +\,1.82\ V$$

From the electrochemical potentials of the two redox systems ($Fe^{2+/3+}$ and Co $^{2+/3+}$), it is convincing that Fe can cause an effective ORR than Co centre as Fe oxidises at a lower potential than cobalt.[11,12] Moreover the +R effect of the S through N atom donates electron density towards Fe enabling facile oxygen adsorption onto Fe centre (as shown in Step-1 of Figure R1). The initiation of ORR occurs via synergistic σ-bonding and π-π non-interacting coupling interactions between the chemisorbed O_2 and active Fe site (square planar d^6 system). This is followed by a series of superoxo and hydroperoxyl intermediates. The alkaline pH used in this study stabilizes the Fe-OOH^- intermediate and the reaction is kinetically primed towards the 4-electron product (OH^-) (Step-2).[13,14] From the electrochemical potential values for Fe and Co redox couples, it is assumed that for the initiation of OER, adsorption of OH^- is favored over Fe (Step-4) with a subsequent partial bridging of the OH^- with the adjacent Co atom and a transient intermediate state is formed with a prevalent electron cloud over the Fe-OH-Co centers (Step-5). This step is crucial to switch over the OER process on the Co active site (square planar d^7 system). The intentional incorporation of electronegative N and S atoms induces electron density towards Co through +R effect (Step-6). The abundance of electrons enables Co to attain the higher oxidation state of +4[15] during the initial stages of OER with a low positive onset potential (Step-7). This is the probable reasons why OER is not favorable on Fe surface, because, owing to a greater Fe-N-S bond distance, (as revealed from XAS data) the electronic interaction for Co is likely to be restricted in the case of Fe where the electronic movement from N and S atoms only negates the positive charge density formed over Fe. The release of dioxygen from Co surface, the rate determining step of OER,[15] is triggered due to the electron drift from Fe (d_{z^2}) to Co (d_{z^2}) enhancing the overall kinetics of the OER process (Step-8,9). Thus, the overpotential $\Delta E_{(ORR\text{-}OER)}$ for the cathode-anode processes is found to be lower in the case of Fe-Co bimetallic system than distinct Fe and Co single metal active centers as strongly evident from the electrochemical data. Therefore, it is clear that the presence of M-N-S moiety in Fe-Co binary metal active center actually triggered the performances of the FeCoDACys electrocatalyst.

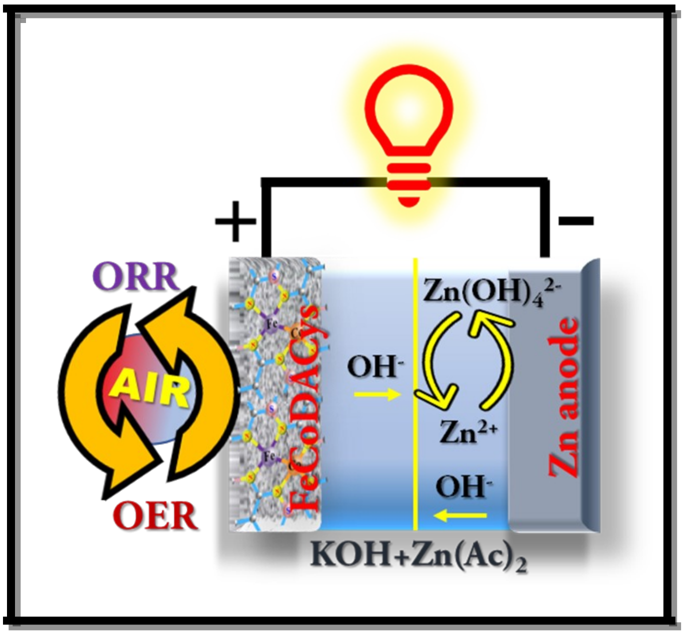

Figure S18: Schematic representation for Zn-air battery assembled in a two-electrode system showing the bifunctional activity of the catalyst.

Table S1. Different parameters obtained from the EXAFS fitting of FeCoDACys catalyst

Scattering Pair	**Coordination (N)**	**R (Å)**
Fe-N	1.88	2.03
Fe-N2	1.11	2.32
Fe-Co	1.23	3.01
Co-N	1.85	2.05
Co-N3	0.8	2.07
Co-Fe	1.15	3.34

N is the coordination number and R is the distance between absorber and back-scattered atoms.

Table S2. Catalysts' performances on the basis of electrocatalytic parameters for ORR and OER.

Catalysts	**Electrolyte**	**$E_{1/2}$ for ORR (V vs RHE)**	**Limiting Current density (J_L) (mA cm^{-2})**	**$E_{j=10\ mA\ cm-2}$ for OER (V vs RHE)**
FeCoDACys	0.1 M KOH for ORR and 1 M KOH for OER	0.74	-5.3	1.53
FeDACys		0.72	-4.29	2.41
CoDACys		0.70	-3.28	1.65
Pt/C		0.85	-5.6	-
RuO_2		-	-	1.43

Table S3. Comparison table of FeCoDACys catalyst with previously reported binary (Fe,Co) metal based bifunctional electrocatalysts

Catalyst	**E_{10} (V vs RHE)**	**$E_{1/2}$ (V vs RHE)**	**ΔE**	**References**
[$Ni_{5.7}Ru_{0.3}(HHTP)_3(H2O)_x$]n	1.62	0.68	0.94	***Chem. Commun.***, 2020,**56**, 13615-13618
3D HNG	1.69	0.95	0.74	*Small Methods* 2018, *2*,1800144
N, P /CoS_2@TiO_2NPFs	1.49	0.91	0.58	*Adv. Funct.Mater. 2018,28, 1804540*
Co-Ni-S@NSPC	1.7	0.82	0.88	*Carbon* 146(2019) 476-485
Co@Co_3O_4@NC-900	1.60	0.8	0.8	*J. Mater.Chem. A*,2018, 6, 1443–1453
Ni_3Fe/N-C sheets	1.60	0.90	0.7	*Adv. EnergyMater. 2017,7, 1601172*
NiFe-LDH/Co,NCNF	1.54	0.79	0.75	*Adv. Energy Mater. 2017,7, 1700467*
B and N dopants (B, N carbon)	1.56	0.88	0.76	*Adv. Sci.* ***2018,*** *5 (7), 1800036.*
N-HC@G-900	1.58	0.72	0.86	*Angew. Chem. Int. Ed.* ***2018,*** *57 (50), 16511-16515.*
Al_2O_3@Co/NG-800	1.58	0.9	0.68	*J. Power Sources* ***2017,*** *353, 28-39.*
$Sm_{0.5}Sr_{0.5}CoO_3$-δ – N Doped Graphene	1.63	0.81	0.82	*Small* ***2018,*** *14 (48), 1802767.*
N-doped ordered mesoporous carbon N-OMC_2	1.72	0.89	0.82	*J. Energy Chem.* ***2017,*** *26 (3), 422-427*
$ZnCo_2O_4$ / rGO	1.55	0.87	0.68	*Int. J. Hydrogen Energ.****2019,*** *44 (3), 1565-1578*
$YBaCo_4O_{7.3}$	1.68	0.68	1	*J. Mater. Chem. A* ***2019,*** *7*

				(1), 330-341.
Co$_3$O$_4$/CNTs	1.54	0.88	0.66	*Sci. Rep.* ***2018,*** *8 (1), 2543*
RuO$_2$	1.79	0.79	1	*Nature Nanotechnol.* ***2015,*** *10, 444.*
NiFeCo-LDH	1.57	0.63	1.05	*Adv.Energy Mater.* ***2015,*** *5 (13), 1500245*
FeCo-ISAs/CN	No OER	0.92	-	*Chem. Commun., 2018,54, 4274-4277*
(Fe,Co)/CNT	No OER	0.881	-	*Energy Environ. Sci., 2018,11, 3375-3379*
N-GCNT/FeCo-3	1.73	0.92	0.81	*Adv. Energy Mater. 2017, 1602420*
FeCo/N-DNC	1.62	0.81	0.81	*Nanoscale 2018, 10, 19937*
FeCo/NPC	1.68	0.81	0.87	*ChemElectroChem 2019, 6, 1824*
FeCo@NCNS	1.597	0.827	0.772	*Electrochim. Acta 2020, 335, 135647*
CoFe/N-GCT	1.66	0.78	0.88	*Angew. Chem. Int. Ed. 2018, 57, 16166 –16170*
FeCoDACys	**1.53**	**0.74**	**0.79**	**This work**

HHTP = 2,3,6,7,10,11-hexhydroxyltriphenylene, 3D Holey N-Doped, NPFs -nanoporous films, NSPC- N, S-doped porous carbon, NC- N-doped carbon, LDH-Layered double hydro oxide, NCNF- N-codoped carbon nanoframes, HC-Holey carbon, NG- D nitrogen-doped graphene, N-OMC- N-containing ordered mesoporous carbon, rGO-Reduced graphene oxide, CNTs- Carbon nanotubes.

References

1 Y. Wang, L. Dong, G. Lai, M. Wei, X. Jiang and L. Bai, *Nanomaterials*, 2019, **9**.

2 Z. J. Zhang, Q. Wang, Y. Q. Zhu and X. Y. Chen, *Carbon N. Y.*, 2016, **100**, 564–577.

3 J. Wang, H. Yang, C. Guan, J. Liu, Z. Chen, P. Liang and Z. Shen, *J. Mater. Chem. A*, 2017, **5**, 24602–24611.

4 Z. Yang, Z. Yao, G. Li, G. Fang, H. Nie, Z. Liu, X. Zhou, X. Chen and S. Huang, *ACS Nano*, 2012, **6**, 205–211.

5 Y. Zhang, B. Ouyang, J. Xu, G. Jia, S. Chen, R. S. Rawat and H. J. Fan, *Angew. Chemie - Int. Ed.*, 2016, **55**, 8670–8674.

6 P. Chen, K. Xu, Z. Fang, Y. Tong, J. Wu, X. Lu, X. Peng, H. Ding, C. Wu and Y. Xie, *Angew. Chemie*, 2015, **127**, 14923–14927.

7 S. Sarkar, N. Kamboj, M. Das, T. Purkait, A. Biswas and R. S. Dey, *Inorg. Chem.*, 2020, **59**, 1332–1339.

8 Y. Wang, D. Liu, Z. Liu, C. Xie, J. Huo and S. Wang, *Chem. Commun.*, 2016, **52**, 12614–12617.

9 R. Zhang, S. Cheng, N. Li and W. Ke, *Appl. Surf. Sci.*, 2020, **503**.

10 S. Sarkar, S. S. Sumukh, K. Roy, N. Kamboj, T. Purkait, M. Das and R. S. Dey, *J. Colloid Interface Sci.*, 2020, **558**, 182–189.

11 J. Wang, W. Liu, G. Luo, Z. Li, C. Zhao, H. Zhang, M. Zhu, Q. Xu, X. Wang, C. Zhao, Y. Qu, Z. Yang, T. Yao, Y. Li, Y. Lin, Y. Wu and Y. Li, *Energy Environ. Sci.*, 2018, **11**, 3375–3379.

12 A. J. Bard and L. R. Faulkner, *Electrochemical Methods: Fundamentals and Applications*, Wiley, 2000.

13 W. Li, A. Yu, D. C. Higgins, B. G. Llanos and Z. Chen, *J. Am. Chem. Soc.*, 2010, **132**, 17056–17058.

14 J. Li, S. Ghoshal, W. Liang, M.-T. Sougrati, F. Jaouen, B. Halevi, S. McKinney, G.

McCool, C. Ma, X. Yuan, Z.-F. Ma, S. Mukerjee and Q. Jia, *Energy Environ. Sci.*, 2016, **9**, 2418–2432.

15 S. Lee, C. Hsu, H. M. Chen, X. Hu, A. Moysiadou, S. Lee, C. Hsu, H. M. Chen and X. Hu, *J. Am. Chem. Soc.*, 2020, **142**, 11901-11914.